Intrinsic spin-glass behavior in novel stoichiometric vanadate $KV_{14}Ge_2O_{27}$

Kei Harada, Nao Kudo, and Hirohiko Sato[*]
Department of Physics, Chuo University, 1-13-27 Kasuga, Bunkyo-ku, Tokyo 112-8551, Japan

(Received 6 November 2024; revised 15 January 2025; accepted 21 February 2025; published 10 March 2025)

A new quaternary vanadate, $KV_{14}Ge_2O_{27}$, has been discovered. It crystallizes in a trigonal lattice with a space group $P\overline{3}$ and lattice constants $a = 7.635$ and $c = 9.225$ Å. The network of vanadium ions consists of isolated octahedral clusters and honeycomblike layers. The chemical composition and the electrical conductivity suggest that the valence of the vanadium ions partially fluctuates between +3 and +4. The temperature dependence of the magnetic susceptibility shows strong antiferromagnetic interactions. Irreversibility in the magnetic susceptibility, slow magnetic relaxations, and aging phenomena appear below 16 K, indicating a spin glass state. $KV_{14}Ge_2O_{27}$ is a novel stoichiometric spin glass material without atomic disorder, where the spin glass is caused by the coexistence of geometric frustration and valence fluctuation.

DOI: 10.1103/PhysRevMaterials.9.034404

I. INTRODUCTION

In vanadates, vanadium has a flexibility of oxidation state in a wide range from V^{2+} to V^{5+}. This allows for a variety of chemical or electrochemical reactions, making vanadates promising materials for catalyses, batteries, sensors, and so on [1]. The variety of valence also leads to interesting electronic properties. The number of $3d$ electrons varies from 3 to 0 as the valence of vanadium varies from 2+ to 5+. This results in a wide range of conduction properties from insulating to superconducting states. In addition, vanadates exhibit a diverse range of magnetic properties because the spin quantum number S varies as $3/2$, 1 and $1/2$ for V^{2+}, V^{3+} and V^{4+}, respectively. As in many highly correlated $3d$ transition metal oxides, electrical conduction and magnetism are strongly coupled in vanadates. Therefore, vanadates often exhibit exotic phenomena caused by the coexistence or competition of spin, charge, and lattice degrees of freedom.

Both of the binary vanadates V_2O_3 and VO_2 are known for their metal-insulator transitions (MIT). V_2O_3 undergoes a transition from paramagnetic metal to antiferromagnetic insulator as a function of temperature, doping, and pressure [2]. This transition can be classified as a Mott transition triggered by electron-electron interactions. On the other hand, the MIT in VO_2 has the character of a Peierls transition, where the electron-lattice coupling plays an important role [3,4]. A further variety of electronic and magnetic properties occurs in ternary vanadates. The vanadium bronze α'-NaV_2O_5, exhibiting quasi one-dimensional magnetism at higher temperatures, undergoes a phase transition to a nonmagnetic state reminiscent of a spin-Peierls transition [5,6]. Detailed studies revealed that the nonmagnetic phase is actually a charge-ordered state [7] as opposed to a bond-ordered spin-Peierls state. Furthermore, pressure induces a series of charge-ordering patterns, whose interesting phase diagram is called the "devil's flower" [8]. Another phase of vanadium bronze, β-$A_{0.33}V_2O_5$ (A = Li, Na, and Ag), undergoes an MIT accompanied by a charge ordering [9]. Under high pressure, the insulating phase is suppressed and superconductivity appears instead [10,11].

In higher symmetry vanadates, the orbital degree of freedom often plays an important role due to the degeneracy of the t_{2g} orbitals of the octahedrally coordinated vanadium ion. For example, the MIT in the hollandite type $K_2V_8O_{16}$ [12] is interpreted in terms of a charge ordering accompanied by an orbital ordering [13]. The spinel-type vanadate MnV_2O_4 undergoes a structural transition from a high temperature cubic phase to a low temperature tetragonal phase, accompanied by the appearance of ferrimagnetism. It has been clarified that an orbital ordering occurs simultaneously with the phase transition [14,15].

In some vanadates, three V^{3+} ions tend to form a triangular cluster through the formation of "bonds" of the t_{2g} orbitals. For example, $LiVO_2$, which has a regular triangular lattice of V^{3+} ions at high temperature, undergoes a structural phase transition with lattice distortion, forming triangular V_3 clusters [16,17]. The magnetic susceptibility disappears in the low temperature phase, indicating a spin singlet ground state on the V_3 "trimers". This phenomenon can be interpreted in terms of the formation of a valence bond solid (VBS). Since the two $3d$ electrons of a V^{3+} ion are involved in forming the "bonding orbitals" to the other two V^{3+} ions, the triangular clusters of V^{3+} ions are particularly stable. Such "trimerization", accompanied by the disappearance of magnetism, is also observed in several other ternary vanadates, such as $AV_{10}O_{15}$ [18,19], $A_2V_{13}O_{22}$ [20], and $AV_{13}O_{18}$ [21] (A = Sr, Ba).

Motivated by the many discoveries of exotic electronic states in ternary vanadates, we have searched quaternary vanadates for novel magnetic and conduction properties. The addition of nonmagnetic elements provides diversity in the magnetic network. In this study, we explored vanadates containing germanium in addition to potassium. Because of the

---

[*] Contact author: shirohiko0011@g.chuo-u.ac.jp

©2025 American Physical Society

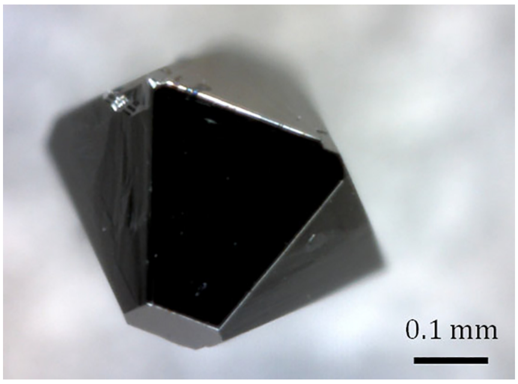

FIG. 1. Micrograph of a single crystal of $KV_{14}Ge_2O_{27}$.

tetrahedral symmetry of the GeO_4 unit, we can expect a highly symmetric crystal structure. In this paper, we report the discovery of a new stoichiometric vanadate $KV_{14}Ge_2O_{27}$ and its intrinsic spin glass (SG) behavior.

II. EXPERIMENTAL

Single crystals of the new vanadate were synthesized by a hydrothermal method. The starting materials, V_2O_3 ($\approx$100 mg) and GeO_2 ($\approx$60 mg), were sealed in a silver capsule with 0.1 mL of KOH solution (2.5 mol/L). Then the capsule was kept at 650 °C and 150 MPa in a test-tube-type autoclave for a few days. The chemical composition was analyzed with an energy-dispersive x-ray spectrometer (EDS) attached to a scanning electron microscope (JEOL, JCM-6000 Plus). The crystal structure was analyzed with a single-crystal x-ray diffractometer (Rigaku, R-Axis RAPID). The electrical conductivity was measured on a single crystal by the DC constant voltage method. The current was measured with ADCMT 5420 ultra-high resistance meter by applying a constant voltage. Magnetization was measured with a superconducting quantum interference device (SQUID) magnetometer (Quantum Design, MPMS-XL).

III. RESULTS

A. Crystal structure

The hydrothermal reaction yielded black crystals. The product was washed with water. The excess GeO_2 and the by-product $K_2V_8O_{16}$ were removed by centrifugation. The typical shape of the crystal is a truncated six-sided bipyramid as shown in Fig. 1. The elemental analysis by EDS revealed the atomic ratio $K : V : Ge = 6 \pm 2 : 83 \pm 2 : 11 \pm 2$.The single-crystal x-ray diffraction study reveals a trigonal lattice with unit cell parameters $a = 7.6347(10)$ and $c = 9.2249(7)$ Å. The initial structure was solved with SHELXT, then the structure was refined with SHELXL [22]. The space group was found to be $P\overline{3}$. The detailed result of the structural analysis can be found in the Supplemental Materials [23]. The summary of the analysis and the atomic positions with the displacement parameters are listed in Table I and Table II.

As shown in Fig. 2, the crystal structure is composed of the VO_6 octahedra, the GeO_4 tetrahedra, and K atoms cuboctahedrally surrounded by twelve O atoms. The VO_6

TABLE I. Crystallographic data of $KV_{14}Ge_2O_{27}$ at 296 K.

Formula	$KV_{14}Ge_2O_{27}$
Crystal color	Black
Crystal system	Trigonal
Space group	$P\overline{3}$
Lattice parameters:	
a (Å)	7.6347(10)
c (Å)	9.2249(7)
Volume (Å^3)	465.67(9)
Z	1
Formula weight	1329.44
Density (calculated) (g/cm^3)	4.740
$2\theta_{\max}$ (deg)	54.7
Number of reflections measured:	
Total	4467
Unique	708
μ (Mo Kα) (cm^{-1})	101.936
Number variables	62
Reflection/parameter ratio	11.42
R [$I > 2.00\sigma(I)$]	0.0455
wR (all reflections)	0.0902
Goodness of fit	1.152

TABLE II. Atomic positions and displacement parameters of $KV_{14}Ge_2O_{27}$ at 296 K.

Atom	Position	x	y	z	B_{eq} (Å^2)
Ge1	2d	0.3333	0.6667	0.44486(14)	0.43(2)
V1	6g	0.04817(16)	0.79823(16)	0.64130(12)	0.47(2)
V2	6g	0.45385(16)	1.08381(17)	0.86661(13)	0.51(2)
V3	2d	0.33333	0.66667	0.8598(2)	0.15(3)
K1	1a	0.0000	1.0000	1.0000	0.94(6)
O1	6g	0.5463(7)	0.7000(7)	1.0020(5)	0.68(7)
O2	6g	0.5127	0.9014(7)	0.7621(5)	0.82(8)
O3	6g	0.2305(7)	1.0434(7)	0.7500(5)	0.62(7)
O4	6g	0.2592(7)	0.8423(7)	0.4952(5)	0.60(7)
O5	2d	0.33333	0.66667	0.2489(8)	0.34(12)
O6	1b	0.0000	1.0000	0.50000	0.9(2)

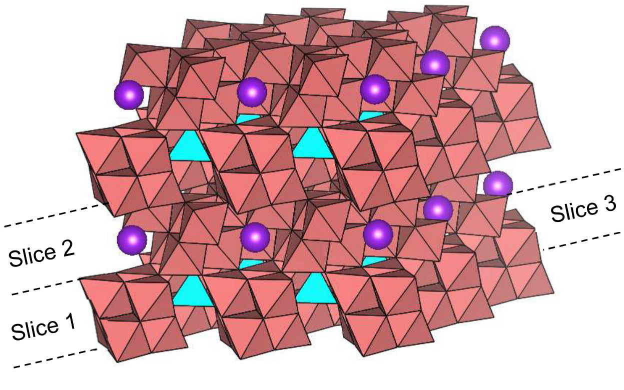

FIG. 2. Crystal structure of $KV_{14}Ge_2O_{27}$. The octahedron and the tetrahedron denote the VO_6 and GeO_4 units, respectively. The sphere denotes a K atom surrounded by 12 O atoms.

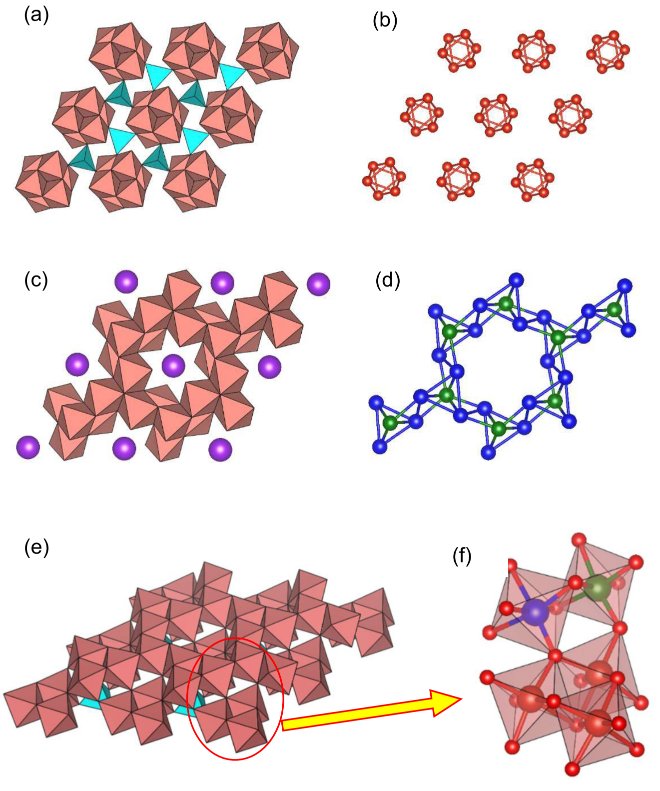

FIG. 3. Details of the crystal structure of $KV_{14}Ge_2O_{27}$. The octahedron, the tetrahedron, and the purple sphere denote VO_6, GeO_4, and K, respectively. To distinguish the three crystallographic vanadium sites, the V1, V2, and V3 sites are indicated by red, blue, and green spheres, respectively. (a) The structure of slice 1. (b) The vanadium network in slice 1. It consists of isolated octahedra of the V1 ions. (c) The structure of slice 2. (d) The vanadium network in slice 2. The V2 and V3 ions form a honeycomb like network. (e) The structure of slice 3. (f) The detail of the connections seen in slice 3. There are edge-shared and vertex-shared connections.

octahedra share their edges or vertices and form a three-dimensional network. The chemical formula of this compound is $KV_{14}Ge_2O_{27}$, in good agreement with the EDS result.

The detailed structures of each "slice" defined in Fig. 2 are shown in Fig. 3. There are three distinct crystallographic sites of vanadium, designated V1, V2, and V3, corresponding to the red, blue, and green spheres in Figs. 3(b), 3(d), and 3(f). Figure 3(a) shows the structure of slice 1 seen from the c axis. It consists of isolated V_6O_{19} clusters composed of six edge-shared VO_6 octahedra. Such a cluster is commonly seen in the polyoxovanadate $[(MCp^*)_4V_6O_{19}]$ (M = Rh, Ir) [24]. The clusters are interconnected by the GeO_4 tetrahedra, which share their vertex oxygens. As shown in Fig. 3(b), the V1 vanadium ions form isolated octahedrons in slice 1. Slice 2 consists of a honeycomblike network of VO_6 octahedra, as shown in Fig. 3(c). All of the adjacent VO_6 octahedra in this slice are connected by sharing their edges. The vanadium network of slice 2 consists of the two crystallographic vanadium sites, V2 and V3, as shown in Fig. 3(d). Figure 3(e) shows the structure of slice 3. Further details of the connections between the octahedra are shown in Fig. 3(f). There are two types of connections, namely edge-shared connections and vertex-shared connections. The vertex-shared connections are seen only in the case of V1–V2 and V1–V3 pairs, while the adjacent V1–V1, V2–V2, and V2–V3 pairs are connected by sharing the edge of their octahedra.

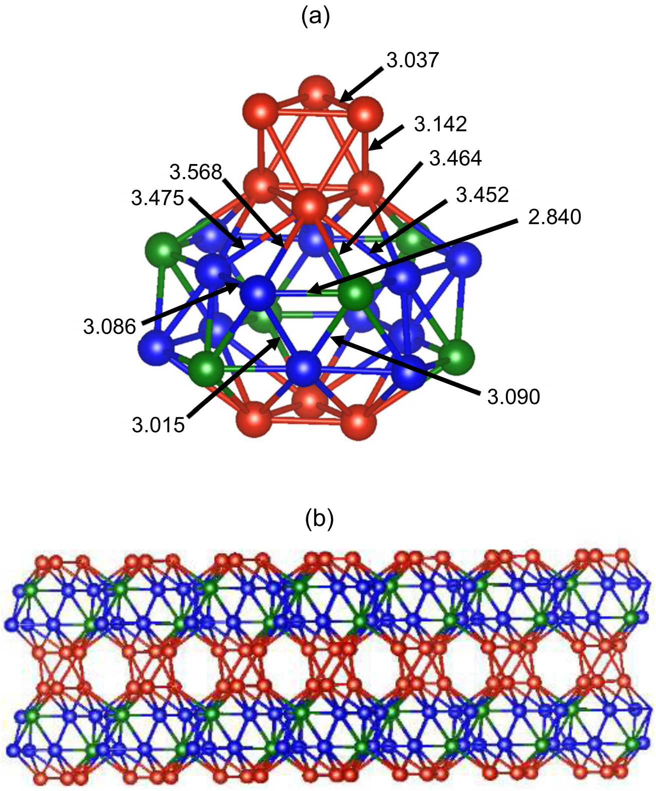

FIG. 4. (a) V–V interatomic distances (in Å unit) in $KV_{14}Ge_2O_{27}$. (b) Network of vanadium ions in $KV_{14}Ge_2O_{27}$. The red, blue, and green spheres denote V1, V2, and V3, respectively.

The octahedrally coordinated V^{3+} and V^{4+} ions have only t_{2g} electrons in the $3d$ orbitals. Unlike the e_g orbitals, the t_{2g} orbitals do not hybridize as much with the $2p$ orbitals of the ligand oxygen atoms. Thus, in vanadate, the exchange interaction arises mainly from direct $t_{2g} - t_{2g}$ overlap of adjacent vanadium ions [17]. The edge-shared connection of VO_6 octahedra is advantageous for the overlap of t_{2g} orbitals, while the direct overlap is less expected in the vertex-shared connection. Therefore, from the point of view of magnetic interactions, the octahedral cluster of six V1 ions is considered to be isolated from the other part. As shown in Fig. 4(a), the interatomic V–V distances vary from 2.840 to 3.568 Å. The V1 ions are significantly distant from the V2 and V3 ions due to the vertex-shared bonds. Figure 4(b) shows the network of vanadium ions. Since the V1–V2 and V1–V3 exchange interactions should be much weaker than those of other pairs, we can view the vanadium network as an alternate stacking of isolated octahedra as in Fig. 3(b) and a honeycomblike sheet as in Fig. 3(d).

The valence of the vanadium ions can be estimated from the compositional formula $KV_{14}Ge_2O_{27}$. Assuming the typical oxidation states K^+, Ge^{4+} and O^{2-}, the average valence of vanadium is calculated to be $\approx +3.21$. The $+45$ charge must be distributed over 14 vanadium sites. This can be realized if 11 and 3 vanadium ions are trivalent and tetravalent,

TABLE III. BVS of vanadium in $KV_{14}Ge_2O_{27}$. The numbers in a bold font are the most reliable BVS values. The values of r_0 are cited from Ref. [25].

Assumed valence	r_0 (Å)	BVS		
		V1	V2	V3
+3	1.743	**2.856**	**2.985**	3.692
+4	1.784	3.190	3.334	**4.125**
+5	1.803	3.359	3.510	4.342

respectively. However, it is incompatible with the structure where the number of crystallographic vanadium sites per formula unit is 6, 6, and 2 for V1, V2, and V3, respectively. This indicates that at least one of the vanadium sites is in a mixed valence state. We also estimated the valence of each vanadium ion from the V–O interatomic distances by calculating the bond valence sum (BVS). The value of BVS of a cation coordinated by anions is defined by

$$\mathrm{BVS} = \sum_i \exp\left(\frac{r_0 - r_i}{B}\right), \tag{1}$$

where B is the empirical constant 0.37 and r_0 is the empirical value depending on the element and its oxidation state [25]. The value r_i is the observed interatomic distance between the cation and the surrounding ith anion. The value BVS is the valence of the cation estimated from the cation–anion bond lengths. Since r_0 depends on the assumed valence of the cation, the BVS closest to the assumption is the most reliable. As shown in Table III, the valences of the V1 and V2 ions are close to +3, while that of the V3 ion is probably +4. This idea is compatible with the compositional formula only if 1/12 of the V1 and V2 ions, that were assumed to be in the V^{3+} state, are actually oxidized to the V^{4+} state. However, it is not possible to identify the oxidized cite as far as this x-ray structure analysis is concerned.

B. Electrical coductivity

The electrical coductivity was measured on a single crystal of $KV_{14}Ge_2O_{27}$ with dimensions of about $0.5 \times 0.5 \times 0.5\ \mathrm{mm}^3$. Due to the small size of the crystal, the conductivity was measured using the two-wire method. The direction of the current could not be accurately determined due to the nearly spherical shape of the crystal. The conductivity at 300 K is $1.4 \times 10^{-2}\ \Omega^{-1}\,\mathrm{cm}^{-1}$ and it decreases with decreasing temperature, indicating a nonmetallic conduction. Figure 5 shows the temperature dependence of the resistivity ρ between 105 and 300 K. The inset shows the $\log \sigma T$ vs T^{-1} plot, where σ is the conductivity.

The nearly linear behavior in the inset of Fig. 5 means that the electrical conduction of $KV_{14}Ge_2O_{27}$ is reproduced by the function

$$\sigma = \frac{\sigma_0}{T} e^{-\frac{E_A}{k_B T}}, \tag{2}$$

suggesting a small-polaron-hopping conduction as in $CuAlO_2$ [26]. In this model, the carriers are localized by the formation of small polarons, where the carriers are self-trapped by the lattice deformation. The structural analysis suggests that one hole carrier is doped for twelve V^{3+} ions in $KV_{14}Ge_2O_{27}$. It is unlikely that the holes are doped to the V1 site because the V_6 octahedra of V1 are so isolated that we would expect poor electrical conduction in this case. Therefore, 1/6 of the V2 sites should be oxidized to V^{4+} and the frequent exchange of V^{4+} and V^{3+} at the V2 sites may lead to the hopping conduction. The magnetic susceptibility shown below also indicates that the holes are probably not doped to the V1 sites. Further measurements of transport properties such as conductivity anisotropy and thermoelectric power will clarify the detailed mechanism of the hopping conduction.

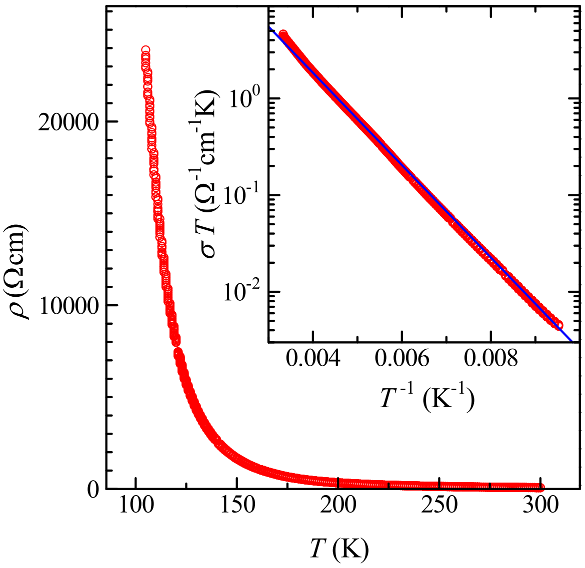

FIG. 5. Temperature dependence of the resistivity of $KV_{14}Ge_2O_{27}$. The inset shows the $\log \sigma T$ vs T^{-1} plot. The red circles are the observed data and the blue line is the best fit using Eq. (2).

C. Magnetism

The magnetization measurements were performed on a 34.7 mg piece of the nonoriented polycrystalline sample. Figure 6(a) shows the temperature dependence of the magnetic susceptibility, which in this paper simply means the magnetization divided by the magnetic field, of $KV_{14}Ge_2O_{27}$ measured in 1 T magnetic field. The core diamagnetism -4.839×10^{-4} emu/mol, calculated using Pascal's constant [27], has already been subtracted from the data. The data may contain a contribution of temperature independent Van Vleck paramagnetism. Note that in V_2O_3 [28], the Van Vleck paramagnetism is estimated to be at most $\approx 10^{-4}$ emu/mol, so we have neglected it in the following analysis. As shown in Fig. 6(b), the susceptibility above about 100 K is almost fitted by a single Curie-Weiss function,

$$\chi = \frac{C}{T - \Theta}. \tag{3}$$

The estimated Curie constant is $C \approx 15$ emu · K/mol. This corresponds to an average g factor of 2.25, assuming that 11 and 3 of the vanadium ions in the composition formula have valences of +3 and +4, respectively. The Weiss temperature

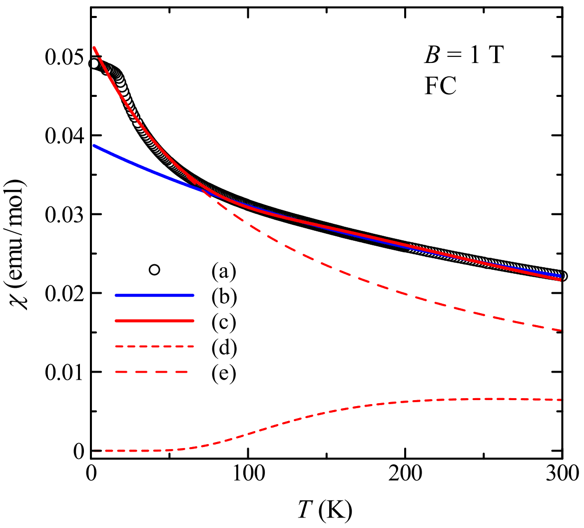

FIG. 6. Magnetic susceptibility of $KV_{14}Ge_2O_{27}$ measured in a field-cooling condition at 1 T of magnetic field. (a) Observed data. (b) Fitting curve based on a single Curie-Weiss model. (c) Fitting curve based on the singlet-triplet model for V1 and the Curie-Weiss model for V2 and V3. (d) Singlet-triplet component of the curve (c). (e) Curie-Weiss component of the curve (c).

Θ is estimated to be $-396\,\mathrm{K}$, suggesting very strong antiferromagnetic interactions.

In the low temperature range below 100 K, the susceptibility deviates upward from the Curie-Weiss model. Although we cannot exclude the possibility that this is due to the change in crystal structure at low temperature, we propose below a simple model that takes into account that V1 ions form isolated clusters.

As shown in Fig. 6(e), the magnetic susceptibility at low temperatures below about 70 K can be reproduced using a Curie-Weiss function with a smaller Curie constant. This suggests that the effective number of magnetic moments decreases at low temperatures. Similar behavior is observed in $La_4Cu_3MoO_{12}$ [29], where the effective number of spins at low temperatures is only 1/3 of that at high temperatures because the cluster of three Cu^{2+} ions behaves as a single $S = 1/2$ spin at low temperatures. The structural study of $KV_{14}Ge_2O_{27}$ indicates that each octahedral cluster of V1 is isolated from the other part. Furthermore, three V^{3+} ions should tend to form a triangular cluster as in $LiVO_2$ [17]. Therefore, we can consider the V1 octahedron as two triangular clusters composed of V^{3+}. In fact, the V–V bond length 3.037 Å within the triangle is significantly shorter than the bond length 3.142 Å between the triangles, as shown in Fig. 4(a). Since the ground state of the $(V^{3+})_3$ trimer should be nonmagnetic, the magnetic contribution of the V1 ions should disappear at low temperature, and only the V2 and V3 ions are responsible for the magnetism in $KV_{14}Ge_2O_{27}$.

From a VBS point of view, an extremely simplified model is to consider the $(V^{3+})_3$ trimer as consisting of three "bonding orbitals" in the ground state, each occupied by two electrons forming a singlet ground state. In the excited state, the electrons occupy the antibonding (triplet) orbitals. In this idea, we can calculate the magnetic susceptibility of the $(V^{3+})_3$ trimer by applying a singlet-triplet model for each bond, resulting in

$$\chi_{\triangle} = 3\frac{2e^{-x}}{1+3e^{-x}}\frac{g^2\mu_{\mathrm{B}}^2}{k_{\mathrm{B}}T}, \tag{4}$$

where

$$x = \frac{2|J|}{k_{\mathrm{B}}T} \tag{5}$$

and J is the exchange interaction between the electrons in each bond. Assuming that the magnetic susceptibility is simply the summation of the cluster magnetism of the V1 ions and the Curie-Weiss magnetism of the V2 and V3 ions, the molar magnetic susceptibility is calculated as

$$\chi = 2N_{\mathrm{A}}\chi_{\triangle} + \frac{C'}{T-\Theta'}. \tag{6}$$

The best-fit susceptibilities using Eq. (6) are plotted in Fig. 6(c). The contributions of the first and second term of Eq. (6) are also shown in Fig. 6(d) and Fig. 6(e), respectively. The optimized parameters are $g = 1.72$, $2|J|/k_{\mathrm{B}} = 410\,\mathrm{K}$, $C' = 6.44$ emu/mol and $\Theta' = -124\,\mathrm{K}$. It reproduces the experimental data very well. The value of C' is very close to 6.12, which is the calculated value of the Curie constant of only V2 and V3 ions, assuming their g values are 2. The value of $\Theta' = -115\,\mathrm{K}$ suggests strong antiferromagnetic interactions in the network of V2 and V3 vanadium ions. The deviation of the g value of the V1 ions from 2 seems too large. This might be due to the oversimplified VBS model in which we ignore the intra-atomic exchange interactions (Hund's rule) and the exchange interactions between the V_3 triangular trimers within the V_6 octahedron.

In the above manner, we have succeeded in reproducing the magnetic susceptibility over a wide temperature range, assuming that the holes are doped only in the V2 sites. If the holes were doped in the V1 sites instead of the V2 sites, the susceptibility would rise steeply at low temperature. This is because the hole doped in the nearly isolated V_6 octahedral cluster would destroy the singlet states, creating an unpaired spin in each cluster. This should cause an additional Curie-type rather than Curie-Weiss-type increase in magnetic susceptibility at low temperature. The absence of such an increase indicates that the holes are doped in the V2 sites rather than the V1 sites. This is consistent with the electrical conduction model where the hole carriers hop among the V2 sites.

Figure 7 shows the magnetic susceptibilities in the low temperature range measured in zero-field-cooled (ZFC) and field-cooled (FC) conditions at 0.02, 0.1, 0.2, 0.5, 1, 2, and 5 T of magnetic fields.At low magnetic fields, the ZFC curve shows a sharp peak, while the FC curve bends at the corresponding temperature and shows no maximum. This irreversible behavior shows that a spin freezing phenomenon such as SG or superparamagnetism occurs at $T_{\mathrm{f}} = 16\,\mathrm{K}$. We can define two characteristic temperatures: T_{max} and T_{irr}. The former is the temperature at which the ZFC curve exhibits a maximum, while the latter is the temperature below which the ZFC and FC curves separate. At low magnetic fields the two temperatures are almost identical to T_{f}. At higher magnetic fields the peak in the ZFC curve becomes less sharp and T_{max} becomes lower while T_{irr} becomes higher. This behavior of T_{max} and T_{irr} is different from that of the typical Ising SG

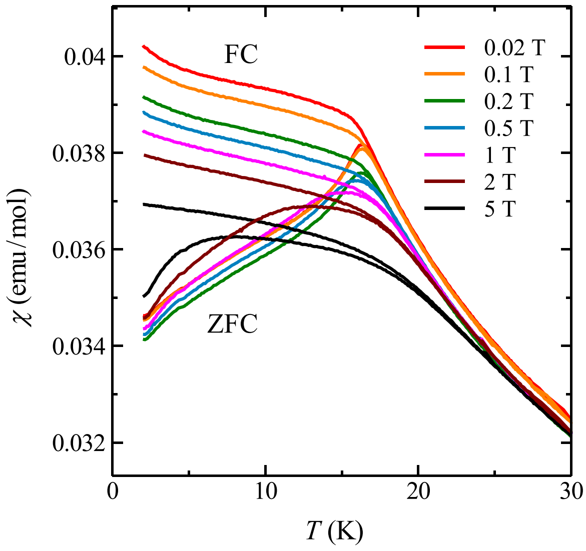

FIG. 7. Magnetic susceptibility of $KV_{14}Ge_2O_{27}$ in the low temperature range measured at various magnetic fields from 0.02 to 5 T. FC and ZFC mean the field-cooled and zero-field-cooled measurements, respectively.

$Fe_xMn_{1-x}TiO_3$ [30] and numerical simulations based on the three-dimensional Edwords-Anderson model [31,32], where T_{irr} becomes lower at higher magnetic fields.

To clarify the origin of the spin freezing phenomenon, time dependence of the magnetization was investigated in two ways. First, the ZFC relaxation was measured by cooling the sample from 30 K to the measurement temperature in the absence of a magnetic field. After a 'waiting time' t_w, a 50 Oe magnetic field was applied and the time dependence of the magnetization was recorded. Figure 8 shows the results of the ZFC relaxation measured at 7 and 12 K. Due to the limitation of the superconducting magnet, it takes 122 s to change the magnetic field. So we have already added 61 s (half of 122 s) to the nominal experimental values of t_w and the time in Fig. 8. Second, the time dependence of the thermoremnant magnetization (TRM) relaxation was also measured, where the sample was cooled from 30 K to the target temperature in 50 Oe of magnetic field. After t_w, the magnetic field was removed and the time dependence of the remnant magnetization was recorded. The results at 7 and 12 K are shown in Fig. 9, where the correction for the response time of the superconducting magnet has already been made.

In both the ZFC relaxation and TRM measurements, the magnetization shows a slow relaxation that lasts for days. Furthermore, the relaxation curves are strongly dependent on t_w. For longer t_w the relaxation is slower. Such an 'aging' phenomenon [33] should not occur in a superparamagnet without interparticle interactions. Thus, the results show that the spin freezing in $KV_{14}Ge_2O_{27}$ results from SG formation. The M vs $\log t$ plots are s-shaped except for $t_w = 1.0 \times 10^5$ s, indicating the existence of an inflection point. Following studies of relaxation phenomena in SGs [34], we attempted to fit the ZFC and TRM relaxation curves with a stretched exponential function

$$M(t) = M_0 \exp\left\{-(t/t_p)^{1-n}\right\} + M_\infty. \tag{7}$$

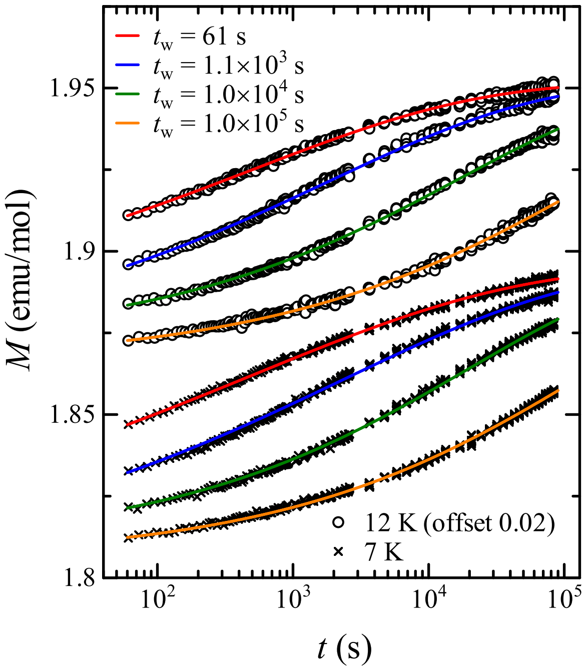

FIG. 8. ZFC relaxation of $KV_{14}Ge_2O_{27}$ at 7 and 12 K. The data at 12 K are shifted up by 0.02 for better visualization. The solid lines are the fitted curves using the stretched exponential function Eq. (7).

The best fit parameters M_0, t_p, n, and M_∞ are listed in Tables IV and V. We assumed that the equilibrium value is unique for each temperature, so that the value of M_∞ is common for all t_w at each temperature. The parameter t_p corresponds to the inflection point of the M vs $\log t$ plots in Fig. 8 or Fig. 9. Obviously, longer t_w will result in longer t_p.

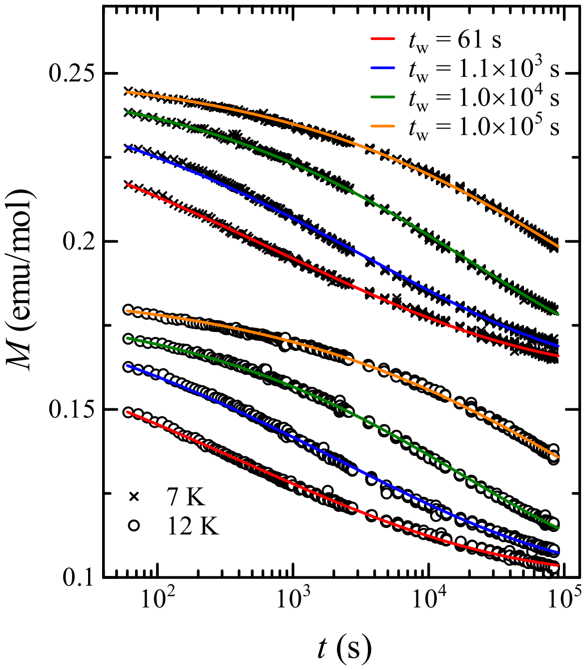

FIG. 9. TRM relaxation of $KV_{14}Ge_2O_{27}$ at 7 and 12 K. The solid lines are the fitted curves using the stretched exponential function Eq. (7).

TABLE IV. Fitting parameters of the stretched exponential model applied to the ZFC relaxations shown in Fig. 8.

T (K)	t_w (s)	M_0 (emu/mol)	t_p (s)	n	M_∞ (emu/mol)
7.0	6.1×10^1	-2.969×10^{-6}	5.005×10^2	0.780	6.186×10^{-5}
7.0	1.1×10^3	-3.106×10^{-6}	2.289×10^3	0.754	6.186×10^{-5}
7.0	1.0×10^4	-2.798×10^{-6}	1.962×10^4	0.667	6.186×10^{-5}
7.0	1.0×10^5	-2.931×10^{-6}	1.443×10^5	0.671	6.186×10^{-5}
12	6.1×10^1	-2.384×10^{-6}	4.921×10^2	0.742	6.305×10^{-5}
12	1.1×10^3	-2.704×10^{-6}	1.796×10^3	0.722	6.305×10^{-5}
12	1.0×10^4	-2.608×10^{-6}	1.702×10^4	0.673	6.305×10^{-5}
12	1.0×10^5	-2.806×10^{-6}	1.472×10^5	0.683	6.305×10^{-5}

Figure 10 shows the relationship between t_w and t_p. Except for the short time region where the data are affected by the slow response of the superconducting magnet, t_w and t_p are almost in the same order of magnitude. This is in agreement with the result for typical SG materials [34].

To study the aging phenomenon in detail, the ZFC aging memory effect [35] was also investigated in the following protocol. The sample was cooled from 30 K to the 'stopping temperature' T_s at a rate of 0.3 K/min in the absence of a magnetic field. After holding the sample at T_s for 5 h, it was cooled again to 2 K at a rate of 0.3 K/min keeping the magnetic field at zero. Then a magnetic field of 50 Oe was immediately applied and the magnetization was recorded while heating at a rate of 0.3 K/min. We performed the experiments with $T_s = 5$, 7, 9.5, and 12 K. The ZFC measurement without temperature holding was also performed for reference. The results are shown in Fig. 11(a). The differences between the hold temperature curves and the ZFC curve are also shown in Fig. 11(b). Each curve shows a dip at about T_s, providing clear evidence of the SG state in this material.

IV. DISCUSSION

The observed behavior of the magnetization below T_f clearly indicates that $KV_{14}Ge_2O_{27}$ is in a SG state. In general, the origins of SGs fall into three main categories. The first is the so-called "canonical" SGs [36], as observed in the *Au*Mn alloy, where the conduction electrons mediate the exchange interactions between the localized spins through the Ruderman-Kittel-Kasuya-Yoshida (RKKY) interaction. Since the sign and magnitude of the RKKY interaction vary greatly as a function of the distance between the localized spins, it often leads to strong competition between the ferromagnetic and antiferromagnetic interactions among the magnetic atoms randomly embedded in the "sea" of delocalized conduction electrons. As a result, the rotation of the spins freezes in a metastable state at low temperatures without the formation of long-range order. The second category are the mixed-crystal insulating SGs. A typical example is the insulating magnet $Fe_{1-x}Mn_xTiO_3$, which is the mixed crystal of $FeTiO_3$ and $MnTiO_3$ [37]. The in-plane magnetic structures are ferromagnetic and antiferromagnetic in $FeTiO_3$ and $MnTiO_3$, respectively. Therefore, there is a competition of the exchange interactions in their mixed crystals due to the randomness. In contrast to canonical SGs, the density of the magnetic atoms is high and the exchange interactions are of a short-range type. Recently, more attention has been paid to the third category of SGs, that is caused by a geometric frustration. In $Y_2Mo_2O_7$, the nearest neighbor interactions between the magnetic Mo^{4+} ions are strongly antiferromagnetic. However, there is no long-range antiferromagnetic ordering, and instead it undergoes a SG transition at 22 K [38,39]. It is not surprising that the geometric frustration of the pyrochlore lattice suppresses a trivial long-range order. However, it is unclear whether geometric frustration alone can induce a SG, since randomness plays a role in conventional SGs. A recent simulation shows that a SG accompanied by an "orbital glass" can arise in stoichiometric $Y_2Mo_2O_7$ without disorder [40].

The conductivity shows that the carriers are localized in $KV_{14}Ge_2O_{27}$, which rules out a SG due to the RKKY interaction in this material. Furthermore, a similar mechanism causing the SG in $Fe_{1-x}Mn_xTiO_3$ is also unlikely in stoichiometric $KV_{14}Ge_2O_{27}$ because of the absence of atomic disorder. SGs have been reported in several stoichiometric compounds other than $Y_2Mo_2O_7$. $Zn_3V_3O_8$ [41] and Fe_2TiO_5 [42,43], which are nominally stoichiometric compounds, exhibit SG behavior. However, their SGs are simply attributed to

TABLE V. Fitting parameters of the stretched exponential model applied to the TRM relaxations shown in Fig. 9.

T (K)	t_w (s)	M_0 (emu/mol)	t_p (s)	n	M_∞ (emu/mol)
7.0	6.1×10^1	3.189×10^{-6}	7.800×10^2	0.771	5.248×10^{-6}
7.0	1.1×10^3	3.035×10^{-6}	3.579×10^3	0.723	5.248×10^{-6}
7.0	1.0×10^4	2.915×10^{-6}	2.099×10^4	0.663	5.248×10^{-6}
7.0	1.0×10^5	2.959×10^{-6}	1.345×10^5	0.673	5.248×10^{-6}
12	6.1×10^1	3.019×10^{-6}	4.222×10^2	0.772	3.280×10^{-6}
12	1.1×10^3	2.998×10^{-6}	2.332×10^3	0.739	3.280×10^{-6}
12	1.0×10^4	2.653×10^{-6}	1.788×10^4	0.654	3.280×10^{-6}
12	1.0×10^5	2.801×10^{-6}	1.301×10^5	0.679	3.280×10^{-6}

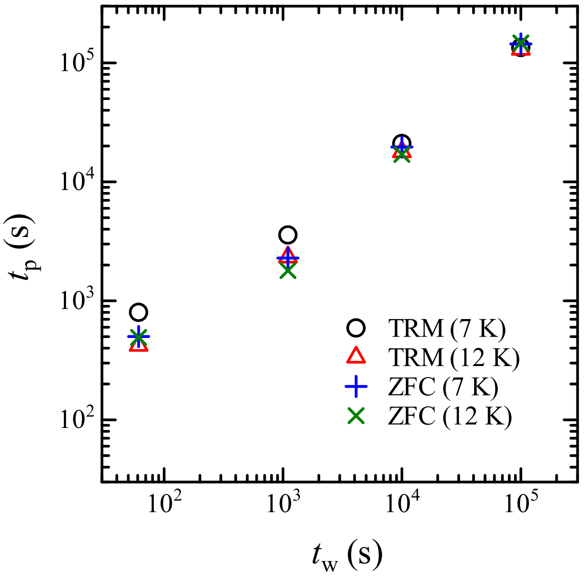

FIG. 10. Relationship between the waiting times t_w and t_p, the latter corresponding to the inflection point of the fitted curves in Figs. 8 and 9.

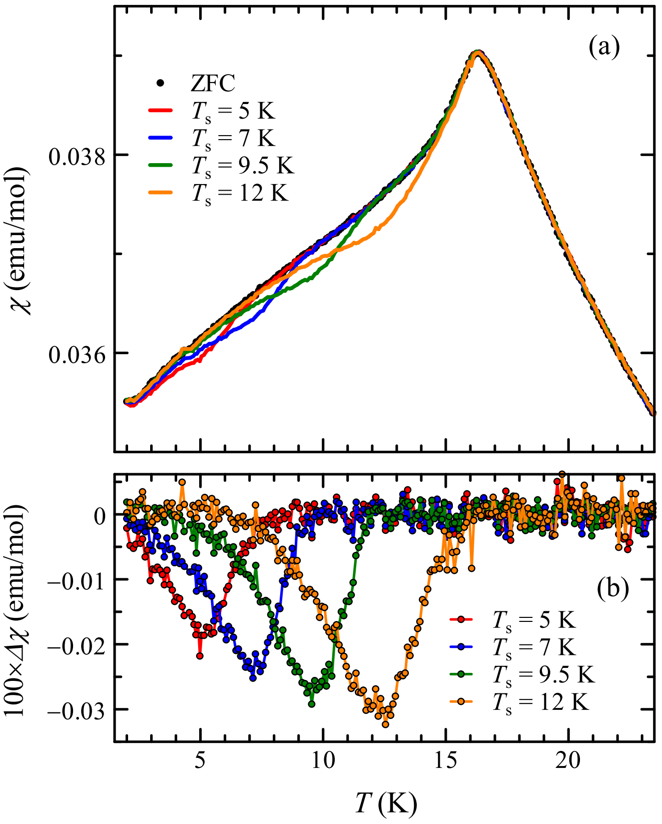

FIG. 11. ZFC aging memory effect of $KV_{14}Ge_2O_{27}$. (a) Magnetic susceptibilities after zero-field-cooling with holding at T_s during cooling. The reference ZFC curve without holding is also measured. (b) The differences $\Delta\chi$ between the susceptibilities with 'temperature hold' at T_s and the reference ZFC curve.

atomic disorder. On the other hand, SG behavior is reported in $PrAu_2Si_2$ [44] and Dy_3TaO_7 [45] despite the absence of atomic disorder. In $PrAu_2Si_2$ it was suggested that dynamic fluctuations of the crystal field levels perturb the development of long-range magnetic order, while the origin of the SG in Dy_3TaO_7 is not clear.

From the strongly negative Weiss temperature, we consider that a geometric frustration should be responsible for the SG in $KV_{14}Ge_2O_{27}$ as in $Y_2Mo_2O_7$. In order to examine whether there is a geometric frustration in $KV_{14}Ge_2O_{27}$, we propose two simplified views of the magnetic network. As shown in Fig. 4(a), the distance 2.84 Å between the V3 ion and the surrounding three V2 ions is significantly shorter than the others. Although, this is partly due to the shorter V–O length of the V^{4+} ions, let us consider the triangle composed of the V3 ion and the three surrounding V2 ions as a magnetic cluster unit. In this case, the triangles are connected to form an effective honeycomb lattice as shown in Fig. 12(a). Since there are non-negligible V–V connections, we cannot ignore exchange interactions between the next-nearest neighbor triangles. Thus, there can be a geometric frustration in the honeycomb lattice if the antiferromagnetic interactions between the nearest and the next-nearest neighbors compete [46]. Another simplified view is obtained by ignoring the V3 ions. In this case the V2 ions form a "star" lattice, known as a highly frustrated lattice [47].

Yang *et al.* named the SG arising mainly from a geometric frustration a 'spin jam' and distinguished it from the conventional SGs [48]. The spin jam has an almost flat rough-bottom energy landscape, while the conventional SGs have a hierarchical funnel type one [49]. The Monte Carlo simulation suggests that the ZFC aging memory effect is weaker, i.e., the dip is shallower and wider in a spin jam than in conventional SGs due to the nearly flat energy landscape. To compare the strength of the ZFC aging memory effect in $KV_{14}Ge_2O_{27}$ with that of other SG materials, we estimated the sharpness of the dips in 11(b) by measuring the 'normalized width' $\Delta T_d/T_f$, where ΔT_d is the full width of the dip at half depth. Figure 13 summarizes the normalized widths of $KV_{14}Ge_2O_{27}$ along with several SGs.Although the measurement conditions are not exactly the same for all materials, we can roughly divide them into several groups. The normalized widths of insulating SGs are significantly large compared to those of canonical SGs such as *Cu*Mn and *Ag*Mn alloys. In particular, the normalized widths of the SGs caused by geometric frustration, such as BCGO and $Y_2Mo_2O_7$, are relatively larger, as pointed out by

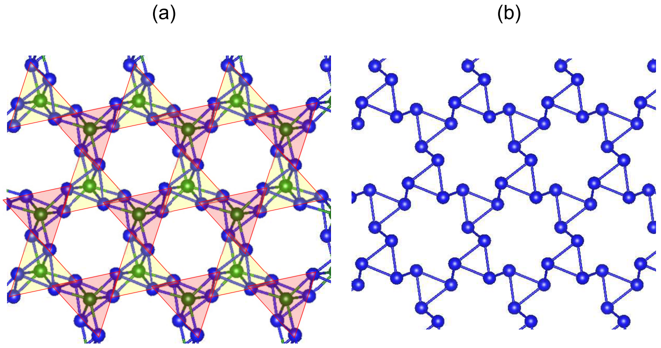

FIG. 12. (a) Honeycomb lattice of the triangular clusters composed of the V2 and V3 ions. (b) Star lattice of V2 ions.

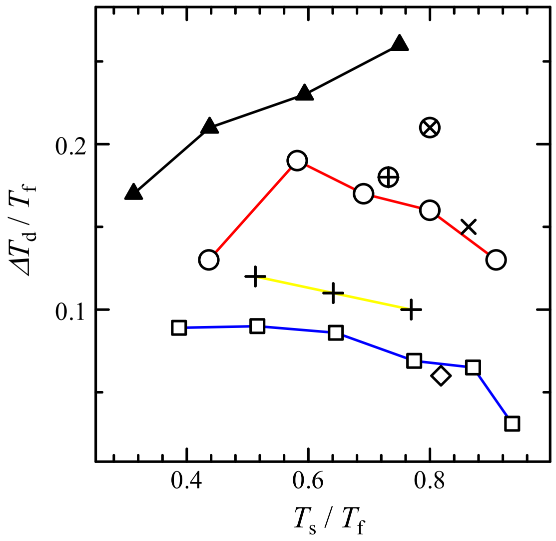

FIG. 13. Normalized dip widths of the ZFC aging memory effect in various SGs. (a) Present material: ▲ $KV_{14}Ge_2O_{27}$. (b) Frustrated SG: ◯ BCGO (p = 0.96) [49], ⊕ $Y_2Mo_2O_7$ [50], ⊗ $ZnFe_2O_4$ [51]. (c) Conventional insulating SGs : × $Fe_{0.55}Mn_{0.45}TiO_3$ [52], + $20Fe_2O_3 \cdot 80TeO_2$ glass [53]. (d) Canonical SGs: □ *Cu*Mn2% [49], ◇ *Ag*Mn [35].

Samarakoon et al [49]. Note that $KV_{14}Ge_2O_{27}$ has the largest normalized dip, suggesting that it has a nearly flat energy landscape like other spin jam systems. This indicates that geometric frustration plays a key role in causing the SG in $KV_{14}Ge_2O_{27}$.

In addition to the geometric frustration, there is a valence fluctuation in $KV_{14}Ge_2O_{27}$ because 1/6 of the V2 ions are oxidized from V^{3+} to V^{4+}. This can disrupt the development of a long-range antiferromagnetic order. In this case, the charge distribution would also be frozen without a long-range order [54]. It is possible that the highly frustrated structure of $KV_{14}Ge_2O_{27}$ also suppresses a charge ordering.

V. CONCLUSION

A novel stoichiometric vanadate $KV_{14}Ge_2O_{27}$ has been discovered. In this material, there are three crystallographic vanadium sites, V1, V2, and V3; the V1 ions form octahedral clusters, while the V2 and V3 ions form honeycomblike layers. The comprehensive study of the structural, electrical, and magnetic properties indicates that the valences of V1 and V3 ions are estimated to be +3 and +4, respectively, while the valence of V2 ions fluctuates between +3 and +4. The magnetization of this material shows irreversibility, slow relaxations, and aging phenomena below 16 K, indicating a SG state despite the absence of atomic disorder. The magnetic susceptibility, indicating strong antiferromagnetic interactions, suggests that the geometric frustration is responsible for the SG. In addition, the charge disorder resulting from the valence fluctuation between V^{3+} and V^{4+} may perturb the development of a trivial antiferromagnetic order. The weakness of the ZFC aging memory effect also suggests that the geometric frustration plays a key role in the SG formation.

Therefore, $KV_{14}Ge_2O_{27}$ is a novel candidate for a "clean" SG material without atomic disorder, in which the SG arises from the coexistence of geometric frustration lattice and valence fluctuation.

ACKNOWLEDGMENTS

The authors thank Professor Hiroko Aruga Katori for valuable suggestions. This study was supported by a Chuo University Personal Research Grant. The drawings of the crystal structures were made by using VESTA [55] software.

---

[1] P. Hu, P. Hu, T. D. Vu, M. Li, S. Wang, Y. Ke, X. Zeng, L. Mai, and Y. Long, Vanadium oxide: Phase diagrams, structures, synthesis, and applications, Chem. Rev. **123**, 4353 (2023).

[2] D. B. McWhan, A. Menth, J. P. Remeika, F. Brinkman, and T. M. Rice, Metal-insulator transitions in pure and doped V_2O_3, Phys. Rev. B **7**, 1920 (1973).

[3] F. J. Morin, Oxides which show a metal-to-insulator transition at the Neel temperature, Phys. Rev. Lett. **3**, 34 (1959).

[4] Y. Muraoka, H. Nagao, Y. Yao, T. Wakita, K. Terashima, T. Yokoya, H. Kumigashira, and M. Oshima, Fermi surface topology in a metallic phase of VO_2 thin films grown on TiO_2(001) substrates, Sci. Rep. **8**, 17906 (2018).

[5] M. Isobe and Y. Ueda, Magnetic susceptibility of quasi-one-dimensional compound α'-NaV_2O_5–Possible spin-Peierls compound with high critical temperature of 34 K–, J. Phys. Soc. Jpn. **65**, 1178 (1996).

[6] Y. Fujii, H. Nakao, T. Yosihma, M. Nishi, K. Nakajima, K. Kakurai, M. Isobe, Y. Ueda, and H. Sawa, New inorganic spin-Peierls compound NaV_2O_5 evidenced by X-ray and neutron scattering, J. Phys. Soc. Jpn. **66**, 326 (1996).

[7] H. Nakao, K. Ohwada, N. Takesue, Y. Fujii, M. Isobe, Y. Ueda, M. V. Zimmermann, J. P. Hill, D. Gibbs, J. C. Woicik, I. Koyama, and Y. Murakami, X-ray anomalous scattering study of a charge-ordered state in NaV_2O_5, Phys. Rev. Lett. **85**, 4349 (2000).

[8] K. Ohwada, Y. Fujii, N. Takesue, M. Isobe, Y. Ueda, H. Nakao, Y. Wakabayashi, Y. Murakami, K. Ito, Y. Amemiya, H. Fujihisa, K. Aoki, T. Shobu, Y. Noda, and N. Ikeda, "Devil's staircase"-type phase transition in NaV_2O_5 under high pressure, Phys. Rev. Lett. **87**, 086402 (2001).

[9] H. Yamada and Y. Ueda, Magnetic, electric and structural properties of β-$A_xV_2O_5$ (A=Na, Ag), J. Phys. Soc. Jpn. **68**, 2735 (1999).

[10] T. Yamauchi, Y. Ueda, and N. Môri, Pressure-induced superconductivity in β-$Na_{0.33}V_2O_5$ beyond charge ordering, Phys. Rev. Lett. **89**, 057002 (2002).

[11] T. Yamauchi and Y. Ueda, Superconducting $\beta(\beta')$-vanadium bronzes under pressure, Phys. Rev. B **77**, 104529 (2008).

[12] M. Isobe, S. Koishi, N. Kouno, J.-I. Yamaura, T. Yamauchi, H. Ueda, H. Gotou, T. Yagi, and Y. Ueda, Observation of

metal-insulator transition in hollandite vanadate, $K_2V_8O_{16}$, J. Phys. Soc. Jpn. **75**, 073801 (2006).

[13] S. Horiuchi, T. Shirakawa, and Y. Ohta, Theoretical study of the electronic states of hollandite vanadate $K_2V_8O_{16}$, Phys. Rev. B **77**, 155120 (2008).

[14] K. Adachi, T. Suzuki, K. Kato, K. Osaka, M. Takata, and T. Katsufuji, Magnetic-field switching of crystal structure in an orbital-spin-coupled system: MnV_2O_4, Phys. Rev. Lett. **95**, 197202 (2005).

[15] T. Suzuki, M. Katsumura, K. Taniguchi, T. Arima, and T. Katsufuji, Orbital ordering and magnetic field effect in MnV_2O_4, Phys. Rev. Lett. **98**, 127203 (2007).

[16] K. Imai, H. Sawa, M. Koike, M. Hasegawa, and H. Takei, Superstructure analyses on single crystals of $Li_{0.8}VO_2$, J. Solid State Chem. **114**, 184 (1995).

[17] H. F. Pen, J. van den Brink, D. I. Khomskii, and G. A. Sawatzky, Orbital ordering in a two-dimensional triangular lattice, Phys. Rev. Lett. **78**, 1323 (1997).

[18] T. Kajita, T. Kanzaki, T. Suzuki, J. E. Kim, K. Kato, M. Takata, and T. Katsufuji, Opening of a charge gap with V trimerization in $BaV_{10}O_{15}$, Phys. Rev. B **81**, 060405(R) (2010).

[19] T. Kajita, H. Kuwahara, S. Mori, and T. Katsufuji, Superstructures arising from V trimers with orbital ordering in $BaV_{10}O_{15}$, Phys. Rev. Res. **3**, 033046 (2021).

[20] J. Miyazaki, K. Matsudaira, Y. Shimizu, M. Itoh, Y. Nagamine, S. Mori, J. E. Kim, K. Kato, M. Takata, and T. Katsufuji, Formation of a three-dimensional network of V trimers in $A_2V_{13}O_{22}$ ($A = $ Ba, Sr), Phys. Rev. Lett. **104**, 207201 (2010).

[21] M. Ikeda, Y. Nagamine, S. Mori, J. E. Kim, K. Kato, M. Takata, and T. Katsufuji, Phase transitions and the role of vanadium t_{2g} states in $AV_{13}O_{18}$ ($A = $ Sr, Ba), Phys. Rev. B **82**, 104415 (2010).

[22] G. M. Sheldrick, A short history of SHELX, Acta Crystallogr. Sect. A: Found. Crystallogr. **64**, 112 (2008).

[23] See Supplemental Material at http://link.aps.org/supplemental/10.1103/PhysRevMaterials.9.034404 for the details of the structural analysis summarized in CIF format.

[24] Y. Hayashi, Y. Ozawa, and K. Isobe, Site-selective oxygen exchange and substitution of organometallic groups in an amphiphilic quadruple-cubane-type cluster. Synthesis and molecular structure of $[(MCp^*)_4V_6O_{19}]$ ($M = $ Rh, Ir), Inorg. Chem. **30**, 1025 (1991).

[25] N. E. Brese and M. O'Keffe, Bond-valence parameters for solids, Acta Crystallogr. B **47**, 192 (1991).

[26] B. J. Ingram, T. O. Mason, R. Asahi, K. T. Park, and A. J. Freeman, Electronic structure and small polaron hole transport of copper aluminate, Phys. Rev. B **64**, 155114 (2001).

[27] G. A. Bain and J. F. Berry, Diamagnetic corrections and Pascal's constants, J. Chem. Educ. **85**, 532 (2008).

[28] D. J. Arnold and R. W. Mires, Magnetic susceptibilities of metallic V_2O_3 single crystals, J. Chem. Phys. **48**, 2231 (1968).

[29] D. A. Vander Griend, S. Boudin, V. Caignaert, K. R. Poeppelmeier, Y. Wang, V. P. Dravid, M. Azuma, M. Takano, Z. Hu, and J. D. Jorgensen, $La_4Cu_3MoO_{12}$: A novel cuprate with unusual magnetism, J. Am. Chem. Soc. **121**, 4787 (1999).

[30] H. Aruga Katori and A. Ito, Experimental study of the de Almeida-Thouless line by using typical Ising spin-glass $Fe_xMn_{1-x}TiO_3$ with $x = 0.41, 0.50, 0.55$ and 0.57, J. Phys. Soc. Jpn. **63**, 3122 (1994).

[31] P. Erika Jönsson and T. Takayama, "Glassy Dynamics" in Ising spin glasses –experiment and simulation–, J. Phys. Soc. Jpn. **74**, 1131 (2005).

[32] H. Takayama and K. Hukushima, Computational experiment on glassy dynamic nature of field-cooled magnetization in Ising spin-glass model, J. Phys. Soc. Jpn. **76**, 013702 (2007).

[33] J. A. Mydosh, *Spin Glasses: An Experimental Introduction* (Taylor & Francis, London, 1993).

[34] P. Nordblad, P. Svedlindh, L. Lundgren, and L. Sandlund, Time decay of the remanent magnetization in a Cu*Mn* spin glass, Phys. Rev. B **33**, 645 (1986).

[35] R. Mathieu, P. Jönsson, D. N. H. Nam, and P. Nordblad, Memory and superposition in a spin glass, Phys. Rev. B **63**, 092401 (2001).

[36] V. Cannella and J. A. Mydosh, Magnetic ordering in gold-iron alloys, Phys. Rev. B **6**, 4220 (1972).

[37] A. Ito, H. Aruga, E. Toritani, M. Kikuchi, Y. Syono, and H. Takei, Time-dependent phenomena in a short-range Ising spin-glass, $Fe_{0.5}Mn_{0.5}TiO_3$, Phys. Rev. Lett. **57**, 483 (1986).

[38] M. J. P. Gingras, C. V. Stager, N. P. Raju, B. D. Gaulin, and J. E. Greedan, Static critical behavior of the spin-freezing transition in the geometrically frustrated pyrochlore antiferromagnet $Y_2Mo_2O_7$, Phys. Rev. Lett. **78**, 947 (1997).

[39] J. S. Gardner, B. D. Gaulin, S.-H. Lee, C. Broholm, N. P. Raju, and J. E. Greedan, Glassy statics and dynamics in the chemically ordered pyrochlore antiferromagnet $Y_2Mo_2O_7$, Phys. Rev. Lett. **83**, 211 (1999).

[40] K. Mitsumoto, C. Hotta, and H. Yoshino, Spin-orbital glass transition in a model of a frustrated pyrochlore magnet without quenched disorder, Phys. Rev. Lett. **124**, 087201 (2020).

[41] T. Chakrabarty, A. V. Mahajan, and S. Kundu, Cluster spin glass behavior in geometrically frustrated $Zn_3V_3O_8$, J. Phys.: Condens. Matter **26**, 405601 (2014).

[42] P. G. LaBarre, D. Phelan, Y. Xin, F. Ye, T. Besara, T. Siegrist, S. V. Syzranov, S. Rosenkranz, and A. P. Ramirez, Fluctuation-induced interactions and the spin-glass transition in Fe_2TiO_5, Phys. Rev. B **103**, L220404 (2021).

[43] Y. Li, P. G. LaBarre, D. M. Pajerowski, A. P. Ramirez, S. Rosenkranz, and D. Phelan, Neutron scattering study of fluctuating and static spin correlations in the anisotropic spin glass Fe_2TiO_5, Phys. Rev. B **107**, 014405 (2023).

[44] E. A. Goremychkin, R. Osborn, B. D. Rainford, R. T. Macaluso, D. T. Adroja, and M. Koza, Spin-glass order induced by dynamic frustration, Nat. Phys. **4**, 766 (2008).

[45] J. F. Gómez-García, L. Bucio, and G. Tavizon, Dy_3TaO_7, A stoichiometric spin glass and the effect of disorder via chemical substitution in the $Dy_{3-x}Y_xTaO_7(0 \leqslant x \leqslant 3)$ solid solution, J. Solid State Chem. **257**, 49 (2018).

[46] S. Katsura, T. Ide, and T. Morita, The ground states of the classical heisenberg and planar models on the triangular and plane hexagonal lattices, J. Stat. Phys. **42**, 381 (1986).

[47] H. Ishikawa, Y. Ishii, T. Yajima, Y. H. Matsuda, K. Kindo, Y. Shimizu, I. Rousochatzakis, U. K. Rößler, and O. Janson, Geometric frustration and Dzyaloshinskii-Moriya interactions in a quantum star lattice hybrid copper sulfate, Phys. Rev. B **109**, L180401 (2024).

[48] J. Yang, A. Samarakoon, S. Dissanayake, H. Ueda, I. Klich, K. Iida, D. Pajerowski, N. P. Butch, Q. Huang, J. R. D. Copley, and S.-H. Lee, Spin jam induced by quantum fluctuations in

a frustrated magnet, Proc. Natl. Acad. Sci. USA **112**, 11519 (2015).

[49] A. Samarakoon, T. J. Sato, T. Chen, G.-W. Chern, J. Yang, I. Klich, R. Sinclair, H. Zhou, and S.-H. Lee, Aging, memory, and nonhierarchical energy landscape of spin jam, Proc. Natl. Acad. Sci. USA **113**, 11806 (2016).

[50] V. Dupuis, E. Vincent, J. Hammann, J. E. Greedan, and A. S. Wills, Aging and memory properties of topologically frustrated magnets, J. Appl. Phys. **91**, 8384 (2002).

[51] M. A. Hakim, M. M. Haque, M. Huq, and P. Nordblad, Spin-glass-like ordering in the spinel $ZnFe_2O_4$ ferrite, Phys. B: Condens. Matter **406**, 48 (2011).

[52] R. Mathieu, P. E. Jönsson, P. Nordblad, H. Aruga Katori, and A. Ito, Memory and chaos in an Ising spin glass, Phys. Rev. B **65**, 012411 (2001).

[53] H. Akamatsu, K. Tanaka, K. Fujita, and S. Murai, Spin dynamics in $Fe_2O_3 \cdot TeO_2$ glass: Experimental evidence for an amorphous oxide spin glass, Phys. Rev. B **74**, 012411 (2006).

[54] F. Kagawa, T. Sato, K. Miyagawa, K. Kanoda, Y. Tokura, K. Kobayashi, R. Kumai, and Y. Murakami, Charge-cluster glass in an organic conductor, Nat. Phys. **9**, 419 (2013).

[55] K. Momma and F. Izumi, VESTA: A three-dimensional visualization system for electronic and structural analysis, J. Appl. Crystallogr. **41**, 653 (2008).